Ratio Limits of Water Storage and Outflow in Rainfall-runoff Process

Yulong Zhu[a], Yang Zhou[b], Xiaorong Xu[c], Changqing Meng[d], and Yuankun Wang[e*]

[a]Yulong Zhu

School of Water Resources and Hydropower Engineering, North China Electric Power University,

Changping Beinong 2# 102206, Beijing, China. Email: zhuyulong@ncepu.edu.cn

[b]Yang Zhou

School of Water Resources and Hydropower Engineering, North China Electric Power University,

Changping Beinong 2# 102206, Beijing, China. Email: zhouyang@ncepu.edu.cn

[c]Xiaorong Xu

School of Water Resources and Hydropower Engineering, North China Electric Power University,

Changping Beinong 2# 102206, Beijing, China. Email: xxrong@ncepu.edu.cn

[d]Changqing Meng

School of Water Resources and Hydropower Engineering, North China Electric Power University,

Changping Beinong 2# 102206, Beijing, China. Email: els_meng@ncepu.edu.cn

[e*]Yuankun Wang (Corresponding author)

School of Water Resources and Hydropower Engineering, North China Electric Power University,

Changping Beinong 2# 102206, Beijing, China. Email: yuankunw@ncepu.edu.cn

20

21 **Abstract**

22 Through the numerical simulations of the hydrodynamic model, the water storage and discharge are found to

23 be limited to envelope lines and the discharge/water depth process lines during water rising and falling

24 showed a grid-shaped distribution. Furthermore, if a catchment is regarded as a semi-open water storage

25 system, there is a nonlinear relationship between the inside average water depth and the outlet water depth,

26 namely the water storage ratio curve, which resembles the shape of a "plume". In the case of an open channel

27 without considering spatial variability, the water storage ratio curve is limited to three values (i.e., the upper,

28 the steady, and the lower limit), which are found to be independent of meteorological (rainfall intensity),

29 vegetation (Manning's coefficient), and terrain (slope gradient) conditions. Meteorological, vegetation, and

30 terrain conditions only affect the size of the "plume" without changing its shape. Rainfall, especially weak

31 rain (rainfall intensity is less than 5.0 mm h^{-1}) significantly affects the fluctuations of water storage ratio,

32 which can be divided into three modes, that is Mode I during rainfall beginning stage, Mode II during rainfall

33 duration stage, and Mode III during rainfall end stage. Results indicate that the determination of the

34 nonlinear relationship of the water storage ratio curve under different geographical scenarios will provide

35 new ideas for simulation and early warning of floods.

36 **1. Introduction**

37   Flood disaster is a significant global health and economic threat. Disastrous floods have caused millions

38 of fatalities in the twentieth century and billions of dollars direct economic loss each year (Merkuryeva, et al.,

39 2015; Merz, et al., 2021; Ruidas, et al., 2022). Weather prediction-based distributed hydrological/hydraulic

40 models are considered to be an effective strategy for flood forecasting (Ming, et al., 2020). According to

41 statistics (Lee, et al., 2020), from 2001 to 2018, over 2,900 floods caused over 93,000 deaths and over 490

42 billion USD in economic damages worldwide. Based on the daily satellite imagery at 250-metre resolution of

43 the 913 large flood events in the same period, a total inundation area of 2.23 million km², with 255-290

44   million people were estimated directly affected by floods (Tellman, et al., 2021). With the influence of

45   climate change and extreme El Niño events (Ward, et al., 2014; Cai, et al., 2014), flood events caused by

46   extreme precipitation are occurring frequently in many regions around the world (Kirezci, et al., 2020; Najibi

47   and Devineni, 2018; Almazroui, 2020). From 2020 to 2023, catastrophic floods caused by several extreme

48   rainfall events were reported in Germany (Tradowsky, et al., 2023), China (Hsu, et al., 2021), Italy (Valente,

49   et al., 2023), Japan (Kobayashi, et al., 2023), Pakistan (Nanditha, et al., 2023) and other developed or

50   developing countries and regions, even in some desert areas (e.g., Taklimakan Desert (Li and Yao, 2023) and

51   Atacama Desert (Cabré, et al., 2023)). Research shows that under a high emissions scenario, in latitudes

52   above 40º north, compound flooding could become more than 2.5 times as frequent by 2100 compared to

53   present (Bevacqua, et al., 2020). It means that in future, the fraction of the global population at risk of floods

54   will be growing.

55   Flood simulation provides an effective means of flood forecasting to reduce property and life losses in

56   flood-threatened areas around the world. A large number of scholars are committed to shortening the

57   simulation time of floods. Accordingly, they have developed many forms of hydrological models (e.g.,

58   Stanford Watershed Model IV (SWM) (Crawford and Linsley, 1966), SHE/MIKESHE model (Abbott, et al.,

59   1986), Tank model (Sugawara, 1995), Soil and Water Assessment Tool (SWAT) (Arnold and Williams, 1987),

60   TOPMODEL (Beven and Kirkby, 1979), etc.), hydrodynamic models (the one-dimension(1D) Saint-Venant

61   equation (Köhne, et al., 2011), the two-dimensions (2D) shallow water equations (SWEs) (Camassa, et al.,

62   1994), and the three-dimensions (3D) integrated equations of runoff and seepage (Mori, et al., 2015)), or

63   coupling models of the two (Kim, et al., 2012; Liu, et al., 2019; Hoch, et al., 2019). Particularly, SWEs are

64   the main governing equations for simulating flood. However, flood simulation based on SWEs is a

65   time-consuming process due to its governing equations are a hyperbolic system of first-order nonlinear

66   partial differential equations (PDEs) (Li and Fan, 2017). Therefore, many scholars attempted to improve the

67 efficiency and accuracy of flood simulation through computer technology ==(GPU parallel computing==

68 ==(Crossley, et al., 2010) or advanced numerical scheme (Sanders, et al., 2010))==. For hydrological studies, the

69 performance of hydrological modeling is usually challenged by model calibration and uncertainty analysis

70 during modeling exercises (Wu, et al., 2021).

71 Hence, we try to ignore the complex exchange/transfer process of mass and momentum (hydrodynamic

72 models), and also abandon the empirical relationships (hydrological models) between the input

73 (precipitation), the transmission (flow rate) and the output (discharge) in the catchment area. A catchment is

74 regarded as a semi-open water storage system. For the storage system, the complex problem is simplified

75 into three megascopic variables, i.e., inflow, water storage and outflow. If we can give a physical-based

76 relationship between the three, flood forecasting will become much simpler.

2. Methods

78 An arbitrary catchment (Fig. 1b) could be assumed to be a conceptual water tank (Fig. 1a). In this water

79 tank, according to the law of conservation of mass, the complex confluence process of surface runoff could

80 be neglected and it can be described only by the relationship between input (average rainfall (R) and

81 exfiltration (-I)), storage (characterized by the internal average water depth (H)), and output (average

82 infiltration (I), evaporation (E), and discharge (Q)), which can be expressed as Eq. 1,

$$\underbrace{A \times \frac{dH}{dt}}_{storage} = \underbrace{R \times A}_{rainfall} \mp \underbrace{\boldsymbol{I \times A}}_{\substack{infiltration \\ /exfiltration}} - \underbrace{E \times A}_{evaporation} - \underbrace{\frac{Q}{A} \times A}_{discharge} \tag{1}$$

84 In this paper, attentions are focused on the surface flow of runoff, so the runoff-atmosphere moisture

85 exchange (evaporation) and runoff-soil moisture exchange (infiltration and/or exfiltration) are

86 non-considered. Zhu et al. (2020) validated the effectiveness of a diffusion wave (DW) approximation of

87 shallow water equations by numerical simulations for simulating ground surface runoff,

$$\frac{\partial h}{\partial t} - \nabla \left(\frac{h^{5/3}}{n_m \sqrt{|S|}} \nabla(h+z) \right) = R \tag{2}$$

89 ==To improve the co==mputational efficiency of hydrodynamic model, after strict mathematical derivation

90   according to the basic hydrodynamic equation and the law of conservation of mass, Zhu et al. (2022)

91   proposed a hydrological-hydrodynamic integrated model, i.e., distributed runoff model (DRM) as,

92
$$\begin{cases} \frac{dH}{dt} = R - q \\ H = \eta h = \eta \left(\frac{n_m}{\sqrt{S}}\right)^{0.6} q^{0.6} \left(\frac{A}{B}\right)^{0.6} \end{cases} \tag{3}$$

93   where, R indicates rainfall intensity (m s^{-1}); q is conceptual outflow (m s^{-1}), $q=Q/A$ (m s^{-1}); n_m is

94   Manning's coefficient (s m$^{-1/3}$); S is the slope gradient; η is the water storage ratio; A is catchment area (m^2)

95   and B is the outlet width (m).
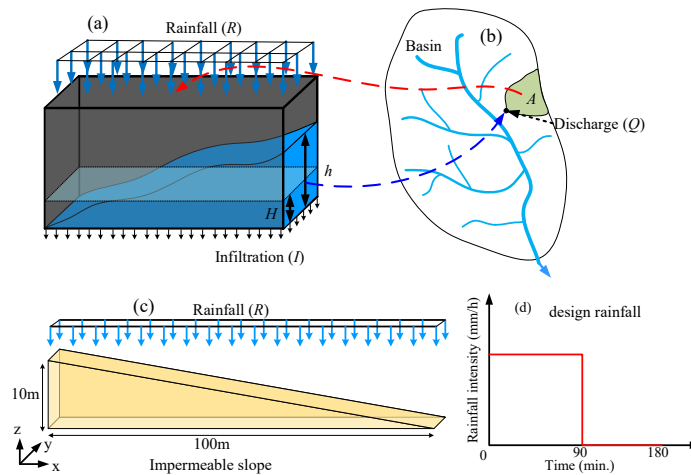
96

97   **Fig. 1. Conceptual schematic of the DRM and numerical model.** (a) conceptual water tank; (b)

98   conceptual catchment; (c) impermeable conceptual slope model; (d) designed rainfall.

99   **3. Limits and "plume" shape of water storage ratio curve**

100   The conceptual hydrological model takes the inside average water depth (H) in the catchment area as

101   the independent variable (Eq. 1). However, the hydrodynamic equations take the water depth at any outlet (h)

102   as an independent variable (Eq. 2). If a relationship between the inside average water depth (H) and outlet

103   water depth (h) can be established, then this relationship will have both hydrodynamic and hydrological

104   characteristics. Therefore, to find the H-h relationship, an impermeable conceptual slope model was built as

105   shown in Fig. 1c and numerical simulations are performed using diffusion wave (DW) approximation (Eq. 2)

106 of shallow water equations (SWEs). The water storage ratio is defined as the inside average water depth (H)

107 divided by the outlet water depth (h). Firstly, the numerical simulations are performed under a designed

108 rainfall condition, i.e., rainfall intensity is 10 mm h^{-1} and rainfall duration are 90 minutes with the total time

109 of 180 minutes as shown in Fig. 1d. From the time-dependent water storage ratio (H/h) under different

110 catchment area (Fig. 2a), it can be seen that the continuous rainfall will cause the water storage ratio (H/h) to

111 gradually decrease from the initial value 1.0 (upper limit) to a stable value, which is approximately 0.625

112 (steady limit). When the rainfall ends, the value of the water storage ratio (H/h) decreases first and then

113 increases, showing a U-shaped curve with a lower limit, which is approximately 0.4125. Afterward, the

114 water storage ratio curves under ten kinds of catchment area (Fig. 2b), three kinds of Manning's coefficient

115 (Fig. 2c), four kinds of slope gradient (Fig. 2d), and four kinds of rainfall intensity (Fig. 2e) conditions are

116 obtained from parametric analyses and summarized in Fig. 2f.
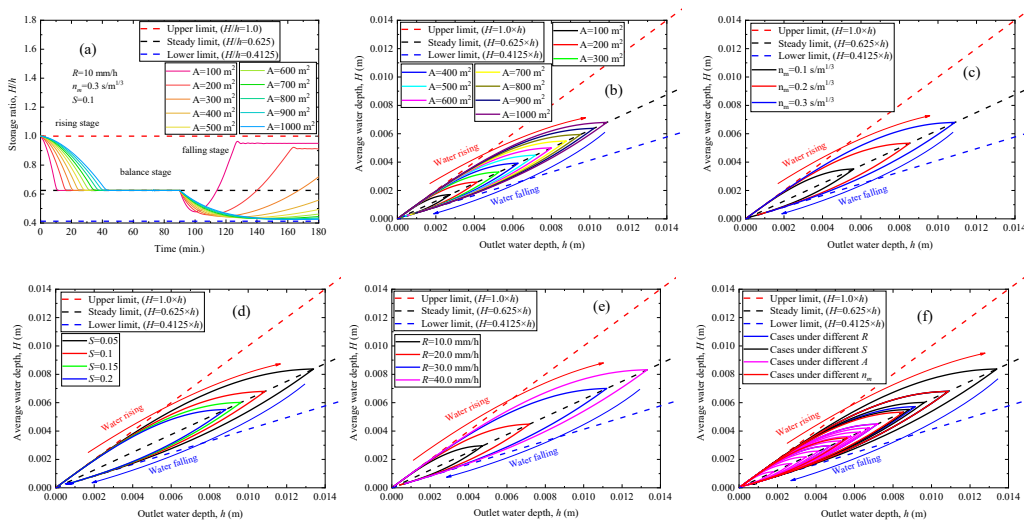
Fig. 2. Water storage ratio curves. (a) Time-dependent water storage ratio under different catchment

area with 10 mm h^{-1}. Water storage ratio curves under different (b) catchment area (A); (c) Manning's

coefficient (n_m); (d) slope gradient (S); and (e) rainfall intensity rainfall intensity (R). (f) Three limit lines

envelop all water storage ratio curves, i.e., Upper limit (H/h=1.0), Steady limit(H/h=0.625), and Lower

123   limit(H/h=0.4125).

124   Finally, it is found that water storage ratio curves resemble a shape of "plume". Higher water storage

125   ratio (H/h) for the water-rising limb than for the water-falling limb at the same outlet water depth.

126   Furthermore, in the case of an open channel without considering spatial variability, there are three limits (the

127   upper, the steady, and the lower limit) of the water storage ratio curves, which are found to be independent of

128   meteorological (rainfall intensity), vegetation (Manning's coefficient), and terrain (slope gradient) conditions.

129   Meteorological, vegetation, and terrain conditions only affect the size of the "plume" without changing its

130   shape that is anchored by three limits. This means that the three limits and the water storage ratio curves

131   provide a key to establish a relationship between the hydrodynamic models and the hydrological models.

132   **4. Grid-shaped cross distribution of discharge/water depth process lines during water rising and**

133   **falling**

134   To obtain further insights into the causes for the formation of the water-rising limb and the water-falling

135   limb of the water storage ratio curve. The ratio of discharge (i.e., the ratio of the total outflows (Q_{out}) to the

136   total inflows (Q_{in}), and the water depth (h) along the slope are discussed in Fig. 3a and Fig. 3b, respectively.

137   Results indicate that there is an envelope line that controls the distribution of the discharge and water depth

138   along the slope, respectively. The discharge envelope line is a straight line with a slope of 1.0 (Fig. 3a), while

139   the water depth envelope line is a nonlinear curve controlled by power function ($h=kx^a$) (Fig. 3b). It means

140   that if the duration of rainfall with a constant intensity is long enough, the catchment system will eventually

141   reach an equilibrium state between inflow and outflow.

142   On the other hand, the process lines of discharge and water depth during water rising and falling present

143   a grid-shaped cross distribution (Fig. 3a and Fig. 3b). Similarly, from the view of the gradient of the

144   discharge and water depth process lines during water rising and falling, the discharge gradient curves (Fig.

145   3c) and the water depth gradient curves (Fig. 3d) also present a grid-shaped cross distribution during water

146 rising and falling, which might be the cause of the looped rating curve (Fig. 3e), i.e., higher discharges for

147 the rising limb (Q_u) than for the recession limb (Q_f) at the same stage (Petersen-Øverleir, 2006). After fitting

148 the value of parameter k and a under different rainfall intensity (R), Manning's coefficient (n_m), and slope

149 gradient (S) conditions (Fig. 3f), it is found that the parameter a is a constant, while the change of parameter

150 k is positively correlated with the change of rainfall intensity (R) and Manning's coefficient (n_m), but

151 negatively correlated with the change of slope gradient (S).
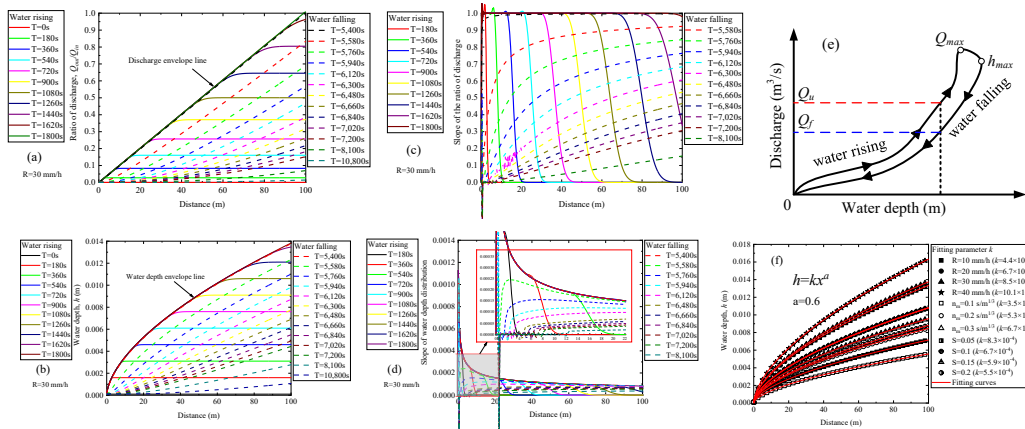
154 **Fig. 3. Discharge/water depth process lines during water rising and falling**. (a) discharge process lines

155 during water rising and falling; (b) gradient lines of discharge process line during water rising and falling; (c)

156 schematic diagram of looped rating curve; (d) water depth process lines during water rising and falling; (e)

157 gradient lines of water depth process lines during water rising and falling; (f) change of water depth envelope

158   line under different rainfall intensity (R), Manning's coefficient (n_m), and slope gradient (S).

159   Based on the water storage ratio curve, a hydrological-hydrodynamic integrated model, namely the

160 Distributed Runoff Model (DRM), is established with the governing equations in Eq. 3. To check the

161 effectiveness and applicability of DRM, the comparative analysis of the numerical results obtained from the

162 DRM and the DW model is implemented. We found that the DRM quickly reproduces the calculation results

163 of the time-consuming DW model under different rainfall intensity (Fig. 4a and Fig. 4b), different Manning's

164 coefficient and different slope gradient (Fig. 4c and Fig. 4d). meaning that the water storage ratio curve will

165   provide new ideas for simulation and early warning of floods. In addition, due to the governing equations od

166   DRM is ordinary differential equations (ODEs), the computational efficiency of DRM is much higher than

167   DW model, which governed by nonlinear partial differential equations (PDEs). More attention should be

168   paid on the determination of the nonlinear relationship of the water storage ratio curve under different

169   geographical scenarios, which will benefit to propose more efficient flood forecasting methods or early

170   warning systems.
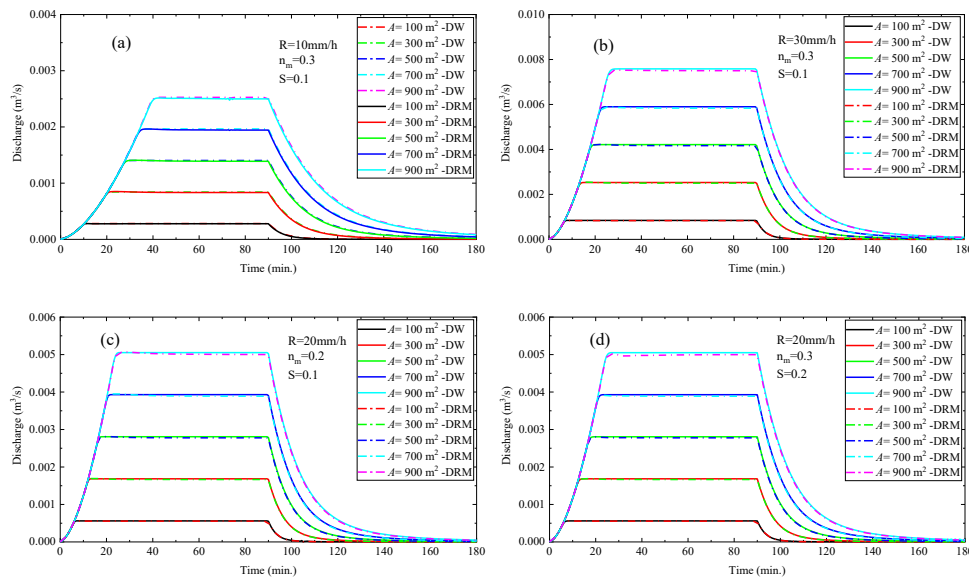
171

172

173   **Fig. 4. Comparative analyses of discharge calculated by DW and DRM under designed rainfall**. (a)

174   controlled group; (b) compared with (a), only the rainfall intensity is changed; (c) compared with (a), rainfall

175   intensity and Manning coefficient are changed; (d) compared with (a), rainfall intensity and slope gradient

176   are changed.

177   **5. Fluctuation of water storage ratio under natural rainfall conditions**

178   After implementing a real rainfall event in the impermeable conceptual slope model (Fig. 1c), the

179   change of the water storage ratio is calculated as shown in Fig. 5. Rainfall data was recorded from 09 August

180   2022 00:00 - 10 August 2022 00:00 in Aomori Prefecture, Japan (https://www.data.jma.go.jp). The total

181   simulation time is 30 hours. Results show that in addition to the fluctuations of water storage ratio in the

182   beginning and end stages of rainfall, there are mainly five fluctuation periods of water storage ratio during

183   the rainfall duration stage, i.e., 1#, 2#, 3#, 4#, and 5# fluctuation (Fig. 5). The fluctuations are found to be

184   mainly caused by weak rainfall ($R<5.0$ mm h^{-1}) as pointed by the red arrows in Fig. 5.
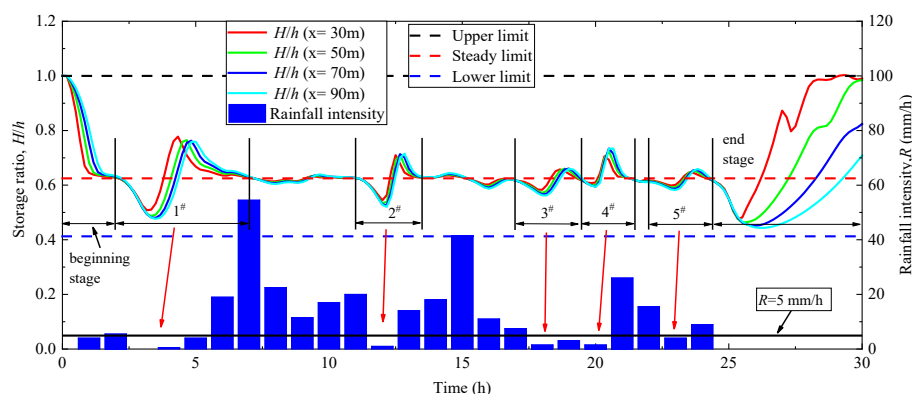
185

186   **Fig. 5. The fluctuation of water storage ratio and the effectiveness of DRM in natural rainfall events**.

187   Besides, the fluctuations of water storage ratio can be divided into three modes, that is Mode I during

188   rainfall beginning stage (Fig. 6a), Mode II during rainfall duration stage (Fig. 6b), and Mode III during

189   rainfall end stage (Fig. 6c). This means that the certainty of the fluctuation modes will provide the possibility

190   for quantitative analysis of the fluctuation of the water storage ratio induced by the change of the rainfall

191   intensity.
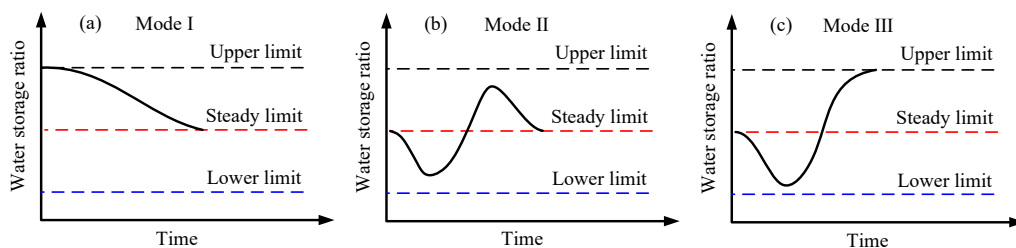
192

193   **Fig. 6. Three kinds of water storage ratio fluctuation mode in natural rainfall events**. (a) water storage

194   ratio fluctuation Mode I during rainfall beginning stage; (b) water storage ratio fluctuation Mode II during

195   rainfall duration stage; (c) water storage ratio fluctuation Mode III during rainfall end stage.

196   Figure 7 shows the simulation results of discharge at different locations calculated by DRM and DW

197   model. Results suggest that after the determination of the water storage ratio fluctuations, the calculation

198   results of DRM are in good agreement with those of DW model, meaning that DRM provides a new and

199   more effective theoretical scheme for flood prediction.
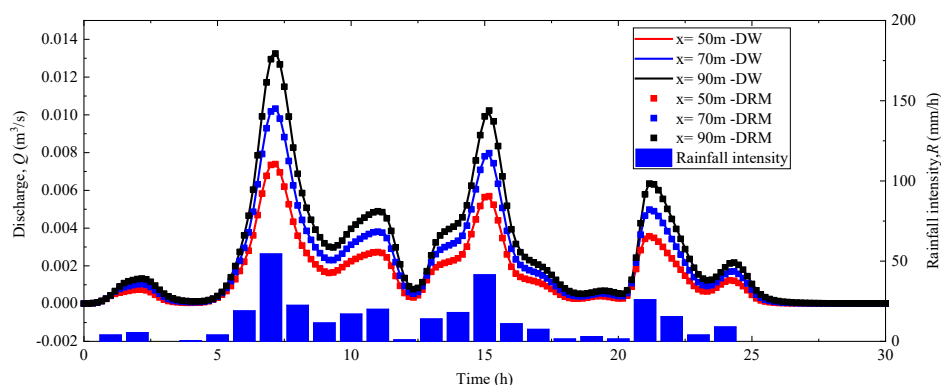
201   **Fig. 7. Time-dependent discharge calculated by DRM and DW model.**

202   **6. Discussions and Conclusions**

203   Through the numerical simulations of the hydrodynamic model, we find that in the rainfall-runoff

204   process, three limits (upper, steady, and lower limit) control the water storage in a catchment, which are

205   independent of meteorological (rainfall intensity), vegetation (Manning's coefficient), and terrain (slope

206   gradient) conditions. The value of the three limits is approximately 1.0, 0.625, and 0.4125, respectively.

207   Under the control of these three limits, a "plume" shaped nonlinear relationship exists between the inside

208   average water depth and the outlet water depth in a catchment, namely the water storage ratio.

209   Meteorological, vegetation, and terrain conditions only affect the size of the "plume" without changing its

210   shape.

211   In addition, the water storage and discharge are limited to envelope lines and the discharge/water depth

212   process lines during water rising and falling showed a grid-shaped distribution, which might be the cause of

213   the looped rating curve, i.e., higher discharges for the rising limb than for the recession limb at the same

214   stage. Rainfall, especially weak rain (rainfall intensity is less than 5.0 mm h^{-1}) significantly affects the

215   fluctuations of water storage ratio, which can be divided into three modes, that is Mode I during rainfall

216   beginning stage, Mode II during rainfall duration stage, and Mode III during rainfall end stage.

217   The findings in this study provide a key to establish a simpler prediction model for floods. Afterward,

218   we constructed a hydrological-hydrodynamic integrated model, namely the Distributed Runoff Model

219   (DRM). Based on a real rainfall event, numerical results indicate that DRM quickly reproduces the

220   calculation results of the time-consuming hydrodynamic model, meaning that the determination of the

221   nonlinear relationship of the water storage ratio curve under different geographical scenarios will provide

222   new ideas for simulation and early warning of floods.

223

Authors' contributions

225   **Yulong Zhu**: Conceptualization, Methodology, Software, Validation, Formal Analysis, Investigation, Data

226   Curation, Writing-Original draft, Writing - Review & Editing.

227   **Yang Zhou**: Methodology, Validation, Investigation, Resources, Data Curation.

228   **Xiaorong Xu**: Methodology, Investigation, Data Curation.

229   **Changqing Meng**: Validation, Investigation, Data Curation.

230   **Yuankun Wang**: Conceptualization, Methodology, Writing-Original draft, Writing - Review & Editing,

231   Supervision, Project administration, Funding acquisition.

232

Availability of data and materials

234   The datasets used and/or analyzed during the current study are available from the corresponding author on

235   reasonable request.

236

237 **Competing interests**

238 The authors declare that they have no conflict of interest.

239

240 **Acknowledgments**

241 This study was supported by National Natural Science Fund of China (52279064) and the Fundamental

242 Research Funds for the Central Universities of China (2021MS043).

243

244 **References**

245 Abbott, M. B., Bathurst, J. C., Cunge, J. A., O'Connell, P. E., and Rasmussen, J.: An introduction to the

246   European Hydrological System-Systeme Hydrologique Europeen,"SHE", 1: History and philosophy of

247   a physically-based, distributed modelling system. Journal of Hydrology, 87(1-2), 45-59,

248   https://doi.org/10.1016/0022-1694(86)90114-9, 1986.

249 Almazroui, M.: Rainfall trends and extremes in Saudi Arabia in recent decades. Atmosphere, 11(9), 964,

250   https://doi.org/10.3390/atmos11090964, 2020.

251 Arnold, J. G., and Williams, J. R.: Validation of SWRRB: Simulator for water resources in rural basins. J.

252   Water Resour. Plan. Manage. ASCE, 113(2), 243-256,

253   https://doi.org/10.1061/(ASCE)0733-9496(1987)113:2(243), 1987.

254 Beven, K. J. and Kirkby, M. J.: A Physically Based Variable Contributing Area Model of Basin Hydrology.

255   Hydrological Sciences Bulletin, 24, 43-69, https://doi.org/10.1080/02626667909491834, 1979.

256 Bevacqua, E., Vousdoukas, M. I., Zappa, G., Hodges, K., Shepherd, T. G., Maraun, D., Mentaschi, L., and

257   Feyen, L.: More meteorological events that drive compound coastal flooding are projected under

258   climate change. Communications Earth & Environment, 1(1), 47,

259   https://doi.org/10.1038/s43247-020-00044-z, 2020.

260   Cabré, A., Remy, D., Marc, O., Burrows, K., and Carretier, S.: Flash floods triggered by the 15-17th March
261   2022 rainstorm event in the Atacama Desert mapped from InSAR coherence time series. Natural
262   Hazards, 116(1), 1345-1353, https://doi.org/10.1007/s11069-022-05707-y, 2023.
263   Cai, W., Borlace, S., Lengaigne, M., van Rensch, P., Collins, M., Vecchi, G., Timmermann, A., Santoso, A.,
264   McPhaden, M. J., Wu, L., England, M. H., Wang, G., Guilyardi, E., and Jin, F. F.: Increasing frequency
265   of extreme El Niño events due to greenhouse warming. Nature Climate Change, 4(2), 111-116,
266   https://doi.org/10.1038/nclimate2100, 2014.
267   Camassa, R., Holm, D. D., and Hyman, J. M.: A new integrable shallow water equation. Advances in Applied
268   Mechanics, 31, 1-33, https://doi.org/10.1016/S0065-2156(08)70254-0, 1994.
269   Crawford, N. H. and Linsley, R. K.: Digital Simulation in Hydrology: Stanford Watershed Model IV.
270   Technical Report No. 39, Department of Civil Engineering, Stanford University, pp. 210, 1966.
271   Crossley, A., Lamb, R., Waller, S., and Dunning, P.: Fast 2D flood modelling using GPU technology-recent
272   applications and new developments. In EGU General Assembly Conference Abstracts, p. 12043, 2010.
273   Hoch, J. M., Eilander, D., Ikeuchi, H., Baart, F., and Winsemius, H. C.: Evaluating the impact of model
274   complexity on flood wave propagation and inundation extent with a hydrologic–hydrodynamic model
275   coupling   framework.   Natural   Hazards   and   Earth   System   Sciences,   19(8),   1723-1735,
276   https://doi.org/10.5194/nhess-19-1723-2019, 2019.
277   Hsu, P. C., Xie, J., Lee, J. Y., Zhu, Z., Li, Y., Chen, B., and Zhang, S.: Multiscale interactions driving the
278   devastating floods in Henan Province, China during July 2021. Weather and Climate Extremes, 39,
279   100541, https://doi.org/10.1016/j.wace.2022.100541, 2023.
280   Kim, J., Warnock, A., Ivanov, V. Y., and Katopodes, N. D.: Coupled modeling of hydrologic and
281   hydrodynamic processes including overland and channel flow. Advances in Water Resources, 37,
282   104-126, https://doi.org/10.1016/j.advwatres.2011.11.009, 2012.

283 Kirezci, E., Young, I. R., Ranasinghe, R., Muis, S., Nicholls, R. J., Lincke, D., and Hinkel, J.: Projections of

284   global-scale extreme sea levels and resulting episodic coastal flooding over the 21st Century. Scientific

285   Reports, 10(1), 11629, https://doi.org/10.1038/s41598-020-67736-6, 2020.

286 Kobayashi, K., Duc, L., Kawabata, T., Tamura, A., Oizumi, T., Saito, K., Nohara, D., and Sumi, T.: Ensemble

287   rainfall–runoff and inundation simulations using 100 and 1000 member rainfalls by 4D LETKF on the

288   Kumagawa River flooding 2020. Progress in Earth and Planetary Science, 10(1), 1-22,

289   https://doi.org/10.1186/s40645-023-00537-3, 2023.

290 Köhne, J. M., Wöhling, T., Pot, V., Benoit, P., Leguédois, S., Le Bissonnais, Y., and Šimůnek, J.: Coupled

291   simulation of surface runoff and soil water flow using multi-objective parameter estimation. Journal of

292   Hydrology, 403(1-2), 141-156, https://doi.org/10.1016/j.jhydrol.2011.04.001, 2011.

293 Lee, J., Perera, D., Glickman, T., and Taing, L. Water-related disasters and their health impacts: A global

294   review. Progress in Disaster Science, 8, 100123, https://doi.org/10.1016/j.pdisas.2020.100123, 2020.

295 Li, M., and Yao, J.: Precipitation extremes observed over and around the Taklimakan Desert, China. PeerJ, 11,

296   e15256, https://doi.org/10.7717/peerj.15256, 2023.

297 Li, P. W., and Fan, C. M.: Generalized finite difference method for two-dimensional shallow water equations.

298   Engineering   Analysis   with   Boundary   Elements,   80,   58-71,

299   https://doi.org/10.1016/j.enganabound.2017.03.012, 2017.

300 Liu, Z., Zhang, H., and Liang, Q.: A coupled hydrological and hydrodynamic model for flood simulation.

301   Hydrology Research, 50(2), 589-606, https://doi.org/10.2166/nh.2018.090, 2019.

302 Merkuryeva, G., Merkuryev, Y., Sokolov, B. V., Potryasaev, S., Zelentsov, V. A., and Lektauers, A.:

303   Advanced river flood monitoring, modelling and forecasting. Journal of Computational Science, 10,

304   77-85, https://doi.org/10.1016/j.jocs.2014.10.004, 2015.

305 Merz, B., Blöschl, G., Vorogushyn, S., Dottori, F., Aerts, J. C., Bates, P., Bertola, M., Kemter, M., Kreibich,

306   H., Lall, U., and Macdonald, E.: Causes, impacts and patterns of disastrous river floods. Nature

307   Reviews Earth & Environment, 2(9), 592-609, https://doi.org/10.1038/s43017-021-00195-3, 2021.

308   Ming, X., Liang, Q., Xia, X., Li, D., and Fowler, H. J.: Real-time flood forecasting based on a high-

309   performance 2-D hydrodynamic model and numerical weather predictions. Water Resources Research,

310   56(7), e2019WR025583, https://doi.org/10.1029/2019WR025583, 2020.

311   Mori, K., Tada, K., Tawara, Y., Ohno, K., Asami, M., Kosaka, K., and Tosaka, H.: Integrated watershed

312   modeling for simulation of spatiotemporal redistribution of post-fallout radionuclides: application in

313   radiocesium fate and transport processes derived from the Fukushima accidents. Environmental

314   Modelling & Software, 72, 126-146, https://doi.org/10.1016/j.envsoft.2015.06.012, 2015.

315   Najibi, N., and Deviveni, N.: Recent trends in the frequency and duration of global floods. Earth System

316   Dynamics, 9(2), 757-783, https://doi.org/10.5194/esd-9-757-2018, 2018.

317   Nanditha, J. S., Kushwaha, A. P., Singh, R., Malik, I., Solanki, H., Chuphal, D. S., Dangar, S., Mahto, S. S.,

318   Vegad, U., and Mishra, V.: The Pakistan flood of August 2022: Causes and implications. Earth's Future,

319   11(3), e2022EF003230, https://doi.org/10.1029/2022EF003230, 2023.

320   Petersen-Øverleir, A.: Modelling looped rating curves. In Proc., XXIV Nordic Hydrological Conf, pp.

321   139-146, https://doi.org/10.13140/2.1.1069.4403, 2006.

322   Ruidas, D., Saha, A., Islam, A. R. M. T., Costache, R., and Pal, S. C.: Development of geo-environmental

323   factors controlled flash flood hazard map for emergency relief operation in complex hydro-geomorphic

324   environment of tropical river, India. Environmental Science and Pollution Research, 30, 106951-106966,

325   https://doi.org/10.1007/s11356-022-23441-7, 2022.

326   Sanders, B. F., Schubert, J. E., and Detwiler, R. L.: ParBreZo: A parallel, unstructured grid, Godunov-type,

327   shallow-water code for high-resolution flood inundation modeling at the regional scale. Advances in

328   Water Resources, 33(12), 1456-1467, https://doi.org/10.1016/j.advwatres.2010.07.007, 2010.

329 Sugawara, M.: The development of hydrological model-tank. Time and the River: essays by eminent

330 hydrologists., 201-258, 1995.

331 Tellman, B., Sullivan, J.A., Kuhn, C., Kettner, A. J., Doyle, C. S., Brakenridge, G. R., Erickson, T. A., and

332 Slayback, D. A.: Satellite imaging reveals increased proportion of population exposed to floods. Nature,

333 596, 80-86, https://doi.org/10.1038/s41586-021-03695-w, 2021.

334 Tradowsky, J. S., Philip, S. Y., Kreienkamp, F., Kew, S. F., Lorenz, P., Arrighi, J., ... and Wanders, N.:

335 Attribution of the heavy rainfall events leading to severe flooding in Western Europe during July 2021.

336 Climatic Change, 176(7), 90, https://doi.org/10.1007/s10584-023-03502-7, 2023.

337 Valente, M., Zanellati, M., Facci, G., Zanna, N., Petrone, E., Moretti, E., Barone-Adesi, F., and Ragazzoni,

338 L.: Health system response to the 2023 floods in Emilia-Romagna, Italy: a field report. Prehospital and

339 Disaster Medicine, 38(6), 813-817, https://doi.org/10.1017/S1049023X23006404, 2023.

340 Ward, P. J., Jongman, B., Kummu, M., Dettinger, M. D., Sperna Weiland, F. C., and Winsemius, H. C.:

341 Strong influence of El Niño Southern Oscillation on flood risk around the world. Proceedings of the

342 National Academy of Sciences, 111(44), 15659-15664, https://doi.org/10.1073/pnas.1409822111, 2014.

343 Wu, H., Chen, B., Ye, X. et al.: An improved calibration and uncertainty analysis approach using a

344 multicriteria sequential algorithm for hydrological modeling. Scientific Reports, 11, 16954,

345 https://doi.org/10.1038/s41598-021-96250-6, 2021.

346 Zhu, Y. L., Ishikawa, T., Subramanian, S.S., and Luo, B.: Simultaneous analysis of slope instabilities on a

347 small catchment-scale using coupled surface and subsurface flows. Engineering Geology, 275, 105750,

348 https://doi.org/10.1016/j.enggeo.2020.105750, 2020.

349 Zhu, Y. L., Zhang, Y. F., Yang, J., Nguyen, B. T., and Wang, Y.: A novel method for calculating distributed

350 water depth and flow velocity of stormwater runoff during the heavy rainfall events. Journal of

351 Hydrology, 612, 128064, https://doi.org/10.1016/j.jhydrol.2022.128064, 2022.